PROCEEDINGS, 51st Workshop on Geothermal Reservoir Engineering
Stanford University, Stanford, California, February 9-11, 2026
SGP-TR-230

Thermo-Hydro-Mechanical Modeling of Cold Front Migration and Microseismic Response in a Fractured Geothermal Reservoir

Le ZHANG *[1,2], Chuanyin JIANG [3], Qinghua LEI [3], Alexandros DANIILIDIS [2], Anne-Catherine DIEUDONNE [2], Longjun DONG [4], Thomas HERMANS [1]

[1] Department of Geology, Ghent University, Ghent, Belgium

[2] Faculty of Civil Engineering and Geosciences, Delft University of Technology, Delft, The Netherlands

[3] Department of Earth Sciences, Uppsala University, Uppsala, Sweden

[4] School of Resources and Safety Engineering, Central South University, Changsha, China

Corresponding author: Le Zhang, Le.zhang@ugent.be

ABSTRACT

Reinjection of cold fluid is essential for sustaining deep geothermal systems but inevitably perturbs the reservoir stress state through coupled thermo-hydro-mechanical (THM) processes, triggering microseismicity. A critical challenge in reservoir management is distinguishing between hydraulic and thermal triggering mechanisms, which tend to exhibit distinct spatiotemporal characteristics. In this study, we investigate the spatiotemporal evolution of induced microseismicity using a fully coupled 2D THM model in conjunction with the discrete fracture network (DFN) approach. By comparing isothermal and non-isothermal injection scenarios, we isolate the specific contributions of poroelastic pressure diffusion and thermoelastic contraction to fracture slip. We find that while pressure perturbations propagate rapidly and induce diffuse, widespread seismicity at early times, the dominant triggering mechanism progressively shifts toward thermoelastic stressing. Analysis of Coulomb failure stress changes (ΔCFS) reveals that cooling-induced instability forms a localized band that co-migrates with the advancing thermal front. Unlike the pressure front, which quickly decouples from the microseismic cloud, the late-time seismic front aligns closely with the cold domain. These findings demonstrate that induced microseismicity is not merely a hydraulic byproduct but can serve as a reliable tracer for cold-front migration, offering a potential tool for forecasting thermal breakthrough in fractured reservoirs.

Keywords: Thermal-hydro-mechanical coupling, Fracture network, Induced seismicity

1. INTRODUCTION

In deep geothermal systems, sustained operation requires reinjection of relatively cold water to maintain circulation and provide pressure support. Injecting cold fluid into hot, fractured rock perturbs pore pressure and temperature fields, and therefore modifies the local stress state (Liu et al., 2025; Zhang, Mi, et al., 2025). Through coupled thermo-hydro-mechanical (THM) processes, these perturbations can reactivate fractures and trigger microseismicity (Chamarczuk et al., 2025; Cuenot et al., 2008; Gaucher et al., 2015). At present, injection-induced microseismicity is primarily treated as an operational uncertainty because it can complicate reservoir management and raise seismic-risk concerns, motivating a better mechanistic understanding of when and where events are likely to occur.

Previous studies have shown that induced seismicity in fractured geothermal reservoirs can arise from multiple triggering mechanisms. Poroelastic pressure diffusion reduces effective normal stress and can promote slip, often accounting for early-time seismicity and a broad spatial expansion of triggered events (Cao et al., 2022, 2024; Jiang et al., 2022). Thermoelastic contraction associated with cooling can also generate localized stress perturbations and alter shear and normal tractions on fractures, and may become increasingly important as the thermal anomaly grows. However, discerning the dominant trigger is challenging because these hydraulic and thermal effects operate concurrently yet evolve differently in space and time. A key complication is that pressure and thermal disturbances may propagate on different time and length scales: pressure can diffuse rapidly through connected fracture pathways, whereas the cold front typically advances more slowly and remains spatially concentrated (Majer et al., 2011; Moein et al., 2023; Rathnaweera et al., 2020). As a result, the pressure front may not uniquely delineate where seismicity clusters at later times, while cooling-induced stresses may organize seismicity into a narrower migrating band. What is still missing is a clear quantitative demonstration using e.g., a coupled process modeling framework to determine whether and when a seismicity front co-migrates with the cold front, and whether such alignment is robust enough to support front tracking from event patterns.

From an operational perspective, this question is directly linked to thermal drawdown control. The position and migration rate of the cold (thermal) front govern heat-sweep efficiency and ultimately determine the timing and extent of thermal breakthrough at producers, yet direct temperature observations are typically limited to wellbores and therefore sparse in space (Ganguly & Mohan Kumar, 2014; Stopa & Wojnarowski, 2006). If the evolving microseismicity is systematically tied to cooling-induced stress changes, event locations and statistics could provide quantitative (although indirect) constraints on cold-front position and migration, enabling improved forecasting and providing a basis for further inversion from seismic catalogs.

In this study, we use a coupled DFN-THM model to compare isothermal and non-isothermal injection under identical hydraulic forcing. We quantify induced slip using fracture seismic moment release, and evaluate Coulomb failure stress change (ΔCFS) to assess the spatiotemporal evolution of failure tendency. By combining cumulative moment evolution with spatial overlays of ΔCFS, pressure/thermal

fronts, and dominant-event locations, we test whether the seismicity front co-migrates with the cold front and assess the feasibility of using microseismicity as a proxy for tracking cold-front migration in fractured geothermal reservoirs.

2. METHODOLOGY

We develop a 2D THM model of a fractured geothermal reservoir using an explicit DFN representation of subsurface fracture systems. The rock matrix is treated as a small-strain thermo-poroelastic material, while fractures are represented as lower-dimensional interfaces embedded in the matrix. Fluid flow and heat transfer evolve in both matrix and fractures, with their interactions captured by matrix–fracture exchange terms. The coupled problem is solved assuming a quasi-static mechanical condition.

2.1 Governing Equations

The matrix permeability is much lower than that of fractures so that the dominant flow pathways are controlled by the fracture network; the reservoir is saturated with water and the flow is treated as single-phase Darcy flow; heat exchange between the fluid within matrix and fractures is described under a local thermal equilibrium framework; and matrix deformation is modeled based on small-strain thermo-poroelasticity.

The quasi-static mechanical equilibrium of the deformable porous medium is governed by

$$\nabla \cdot \boldsymbol{\sigma} + \boldsymbol{f} = \mathbf{0}, \tag{1}$$

where σ is the total stress tensor and f is the body-force vector. The infinitesimal strain is given by

$$\boldsymbol{\varepsilon} = \frac{1}{2}(\nabla \boldsymbol{u} + (\nabla \boldsymbol{u})^T), \tag{2}$$

and the linear thermo-poroelastic constitutive relation is expressed as

$$\boldsymbol{\sigma} = \lambda \mathrm{tr}(\boldsymbol{\varepsilon})\boldsymbol{I} + 2G\boldsymbol{\varepsilon} - \alpha_B p\boldsymbol{I} - 3K\alpha_T \Delta T \boldsymbol{I}, \quad \Delta T = T - T_{\mathrm{ref}}, \tag{3}$$

where u is displacement, λ and G are Lamé's first parameter and shear modulus, K is bulk modulus, α_B is Biot's coefficient, α_T is the linear thermal expansion coefficient, and p and T are pore pressure and temperature.

Fracture deformation and reactivation involve normal closure, frictional shear response, and shear-induced dilation. Let σ_n and τ denote the normal and shear tractions on a fracture (compression positive). The effective normal compressive stress is

$$\sigma_n' = \sigma_n - \alpha_b p_f, \tag{4}$$

where p_f is pore pressure within the fracture and α_b is the Biot coefficient for fractures. Normal closure under compression follows a hyperbolic relation

$$v_n = \frac{\sigma_n' v_m}{K_{n0} v_m + \sigma_n'}, \tag{5}$$

where v_n is the normal closure, K_{n0} is the initial normal stiffness, and v_m is the maximum allowable closure; the corresponding stress-dependent normal stiffness is

$$K_n = \frac{\sigma_n'}{v_n} = \frac{(K_{n0} v_m + \sigma_n')^2}{K_{n0} v_m^2}. \tag{6}$$

The fracture shear behavior is modeled as elastic–perfectly plastic associated with a Coulomb failure criterion

$$\tau_s = \begin{cases} K_s u_s, & u_s < u_p, \\ \tau_p, & u_s \geq u_p, \end{cases} \qquad \tau_p = \sigma_n' \tan \phi_f, \qquad u_p = \frac{\tau_p}{K_s}, \tag{7}$$

where u_s is shear displacement, K_s is shear stiffness, ϕ_f is the friction angle, and u_p is the peak shear displacement beyond which sliding occurs. The irreversible shear-induced dilation is computed incrementally as

$$dv_s = \begin{cases} -\tan \phi_d du_s, & u_s \leq u_r, \\ 0, & otherwise, \end{cases} \tag{8}$$

where ϕ_d is the dilation angle and u_r is the residual shear displacement. The fracture aperture b under combined normal and shear effects is updated as

$$b = \begin{cases} b_0 + w, \sigma_n' < 0, \\ b_0 - v_n - v_s, \sigma_n' \geq 0, \end{cases} \tag{9}$$

where b_0 is the initial aperture and w is the wall separation when the fracture is in tension.

Fluid flow through deformable fractured porous media is modeled in both matrix and fracture domains. In the matrix, the mass conservation equation coupled with Darcy's law is written as

$$\rho_w \left(S_m \frac{\partial p_m}{\partial t} + \alpha_B \frac{\partial \varepsilon_v}{\partial t} \right) - \nabla \cdot (\rho_w v_m) = 0, \quad v_m = -\frac{\kappa_m}{\mu} \nabla p_m, \tag{10}$$

where ρ_w is water density, μ is dynamic viscosity, p_m is matrix pressure, $\varepsilon_v = \mathrm{tr}(\varepsilon)$ is volumetric strain, κ_m is matrix permeability, and v_m is Darcy velocity in matrix. Along fractures, the lower-dimensional mass balance is

$$b\rho_w S_f \frac{\partial p_f}{\partial t} + \rho_w \frac{\partial b}{\partial t} - \nabla\tau \cdot \left(b\rho_w v_f \right) = \rho_w \left(f_{up} + f_{bottom} \right), \qquad uf = -\frac{\kappa_f}{\mu} \nabla\tau p_f, \tag{11}$$

where $\nabla\tau$ denotes the tangential gradient operator on the fracture plane, v_f is Darcy velocity in fracture, κ_f is fracture permeability (related to aperture via the cubic law), and f_{up} and f_{bottom} are exchange fluxes between the fracture and the two adjacent matrix blocks. The exchange term at each fracture wall is expressed as

$$f_i = -\frac{\kappa_m}{\mu} \frac{\partial p_i}{\partial n_i}, \qquad i \in (up, bottom), \tag{12}$$

where n_i is the outward normal direction of the corresponding fracture wall. The storage coefficients for matrix and fractures are

$$S_m = \chi_w + (1 - \alpha_B)(\alpha_B - \phi)\chi_m, \qquad S_f = \chi_w + \frac{1}{K_n b}, \tag{13}$$

where ϕ is matrix porosity, χ_w is water compressibility, and χ_m is the drained compressibility of the rock matrix.

Heat transfer in the rock matrix is governed by an energy balance equation including thermal advection driven by Darcy flow and thermal conduction

$$(\rho C)_{eff} \frac{\partial T_m}{\partial t} + \rho_w C_w u_m \cdot \nabla T_m - \nabla \cdot \left(\lambda_{eff} \nabla T_m \right) = 0, \tag{14}$$

where T_m is matrix temperature, C_w is the specific heat capacity of water, while the effective volumetric heat capacity and thermal conductivity are respectively given by

$$(\rho C)_{eff} = \phi\rho_w C_w + (1 - \phi)\rho_s C_s, \qquad \lambda_{\mathrm{eff}} = \phi\lambda_w + (1 - \phi)\lambda_s, \tag{15}$$

with $\rho_s, C_s,$ and λ_s respectively denoting density, heat capacity, and thermal conductivity of the rock solid (note that the subscript w indicates the same properties for water). For fractures, the energy balance equation is written in a lower-dimensional form as

$$b\rho_w C_w \frac{\partial T_f}{\partial t} + b\rho_w C_w u_f \cdot \nabla\tau T_f - \nabla_\tau \cdot \left(b\lambda_w \nabla\tau T_f \right) = e_{\mathrm{up}} + e_{\mathrm{bottom}}, \tag{16}$$

where T_f is fracture temperature and $e_{\mathrm{up}}, e_{\mathrm{bottom}}$ are the fracture–matrix energy exchange terms at the two fracture walls. The exchange at each wall is expressed as

$$e_i = \rho_w C_w T_i f_i - \lambda_{\mathrm{eff}} \frac{\partial T_i}{\partial n_i}, \qquad i \in (up, bottom), \tag{17}$$

where f_i is the corresponding mass exchange term and n_i is the outward normal direction.

2.2 Model Setting

The numerical model represents a 2D horizontal section of a fractured geothermal reservoir at a depth of 2 km. The fracture system is explicitly represented using a DFN composed of two fracture sets striking at 135° and 60°, comprising 854 fractures in total. The computational domain is 1000 × 1000 m^2, with the injector located at (250,250) m and the producer at (750,750) m. The far-field stress state is prescribed using depth-dependent stress gradients, the initial pore pressure follows a hydrostatic distribution, and the initial temperature is uniform with $T_0 = 180°\mathrm{C}$.

To isolate the role of cooling, we perform two injection scenarios that share identical hydraulic boundary conditions and retain the same fully coupled THM formulation, but differ in the injected fluid temperature (Zhang, Dieudonné, et al., 2025). In the non-isothermal scenario, the injector's temperature is set to $T_{\mathrm{inj}} = 60°\mathrm{C}$, generating a pronounced cooling zone and a migrating thermal front and accommodating significantly thermoelastic stress changes. In the isothermal scenario, the injector's temperature is set equal to the initial

reservoir temperature $T_{\text{inj}} = T_0 = 180°\text{C}$, so that cooling is negligible and the reservoir response is therefore dominated by poroelastic effects.

The flow between the two wells is governed by a pressure gradient of $dp/dL_w = 10$ kPa/m defined over the injector–producer separation (D), such that the injection pressure is set to $p_{\text{inj}} = p_0 + (dp/dL_w)D$ while the production pressure is kept equal to the initial pressure. The domain is discretized using an unstructured triangular mesh with a maximum element size of 10 m, and simulations are run for up to 10^9 s (≈ 31.7 years).

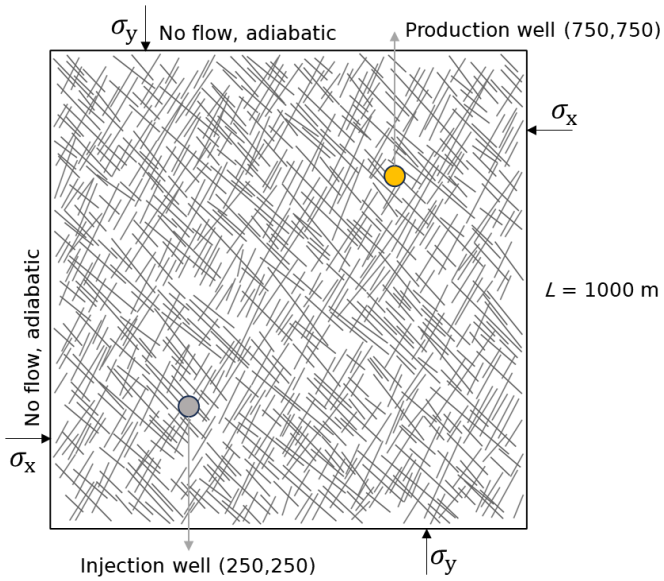

Figure 1: Conceptual model with boundary conditions and DFN configuration.

2.3 Analysis Metrics

To quantify the coupled response and connect simulated slip to observable features, we evaluate (i) seismic-moment release associated with fracture slip, (ii) Coulomb failure stress change on fractures, and (iii) the migration of pressure, thermal, and seismic fronts.

Seismicity is represented by slip on individual fractures. For each fracture, the incremental seismic moment over a time interval $[t_{i-1}, t_i]$ is computed as

$$dM_0^{(i)} = GA|\Delta\bar{u}|, \qquad A = Lh,$$

where G is the shear modulus, L is the length of the fracture, h is the out-of-plane thickness (taken as unity), and $\Delta\bar{u}$ is the fracture slip increment averaged by length during time interval. The cumulative seismic moment at time t_i is defined as the total moment released since the initial state.

We assess fracture failure tendency using the Coulomb failure stress change evaluated directly from the simulated shear traction τ and effective normal stress $\sigma_{n,\text{eff}}$ on each fracture segment:

$$\Delta CFS^{(i)} = (\tau_i - \tau_{i-1}) - \mu\left(\sigma_{n,\text{eff},i} - \sigma_{n,\text{eff},i-1}\right),$$

where $\mu = 0.6$ is the friction coefficient. We adopt the geomechanics sign convention (compression positive for $\sigma_{n,\text{eff}}$), such that positive ΔCFS indicates an increased tendency for slip over the interval.

The thermal front is defined by an isotherm

$$T = T_{\text{front}} = \frac{T_0 + T_{\text{inj}}}{2},$$

and the pressure front is defined by an isobar

$$p = p_{\text{front}} = \frac{p_0 + p_{\text{inj}}}{2},$$

where T_0 and p_0 are respectively the initial reservoir temperature and pressure, and T_{inj} and p_{inj} are respectively the imposed injector temperature and pressure. Event locations shown in maps are represented by the length-weighted centroid of fractures that slip during each interval.

To define a seismic front consistently, fractures are ranked by their incremental seismic moment dM_0 in each interval, and the subset contributing the top fraction q of the total moment release is selected (here q = 25%). The seismic front distance is quantified as a robust characteristic distance from the injector to this selected event set, taken as the 95th percentile of injector-to-event distances. The resulting seismic-front distance is compared with the pressure- and thermal-front distances through time.

3. RESULTS

3.1 Temporal Evolution of Seismic Moment

Figure 2 compares the cumulative seismic moment for the non-isothermal case (solid) and the isothermal case (dashed), where the dotted curve represents the thermal contribution, calculated as the difference between the two. The cumulative moment increases by several orders of magnitude over the simulation, from $\sim 10^8$ N·m at early time to $\gtrsim 10^{12}$ N·m by 10^9 s, and the non-isothermal case releases substantially more seismic energy than the isothermal case, with the separation widening progressively through time.

At early times ($<10^4$ s), the two curves are nearly indistinguishable and the thermal contribution is negligible, indicating that the initial response is dominated by poroelastic effects. Around 10^4 s, the curves begin to diverge as cooling-induced stresses become measurable. And around 10^6 s, the curves diverge as the isothermal reference begins to flatten, indicating the saturation of poroelastic effects. Consequently, thermal stressing becomes the dominant mechanism well before 10^8 s, driving the continued surge in seismic moment while the pressure-driven component stabilizes. This demonstrates that long-term fracture slip in this setting cannot be explained by pore-pressure effects alone.

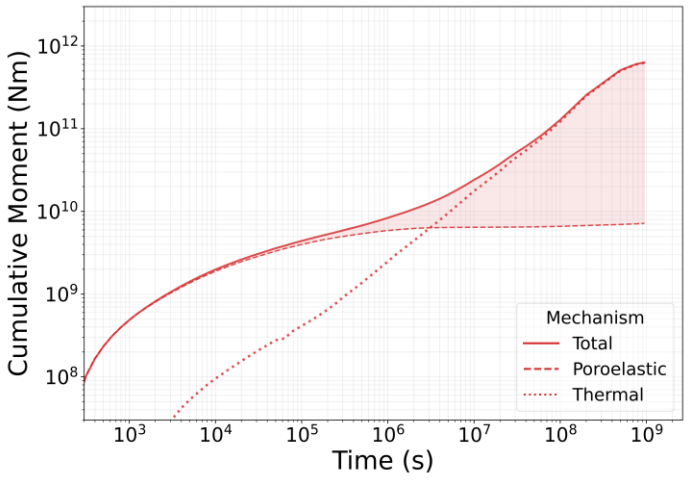

Figure 2: Cumulative seismic moment evolution comparing isothermal and non-isothermal injection scenarios.

3.2 Spatiotemporal Decoupling of Pressure and Thermal Fields

Figure 3 shows plan-view maps of matrix perturbations at three representative times ($t = 10^4, 10^6, 10^8$s). The rows display changes relative to the initial state in pore pressure Δp (top), temperature ΔT (middle), and minimum principal stress $\Delta\sigma_3$ (bottom). For each time, panels compare the isothermal and non-isothermal injections, so that the influence of thermal evolution and thermoelastic coupling can be distinguished from purely poroelastic effects.

Two contrasting spatiotemporal scales are evident. The pressure perturbation propagates rapidly along the connected fracture network at early time, producing fast, pathway-controlled expansion away from the injector. It then quickly evolves into a spatially extensive but relatively diffuse and quasi-stable Δp pattern, reflecting rapid hydraulic communication over a large portion of the domain rather than a persistently localized band. In contrast, the temperature perturbation remains confined to the region swept by the injected cold water and therefore exhibits a much more concentrated footprint. The ΔT field forms a compact cold domain near the injector at early time and subsequently advances outward along preferential pathways, maintaining a narrow, plume-like geometry.

The minimum principal stress perturbation closely mirrors the thermal field. In the non-isothermal case, the strongest $\Delta\sigma_3$ changes occur where cooling is most pronounced, and the spatial extent of $\Delta\sigma_3$ largely overlaps the cold domain defined by ΔT. Regions that experience elevated Δp but little cooling show much weaker changes in $\Delta\sigma_3$, emphasizing that pressure diffusion alone does not generate the same level of concentrated stress perturbations in the matrix.

These observations reflect the different processes governing pressure and temperature. Pressure perturbations propagate efficiently through connected permeability structure and therefore influence a wide area, but this broad footprint does not necessarily translate into

localized stress changes that strongly promote slip. Cooling, in contrast, is controlled by advective transport within preferential fracture pathways and by matrix–fracture heat exchange, which confines the thermal anomaly and induces thermoelastic contraction in a limited region. The close spatial coincidence between the cold domain and $\Delta\sigma_3$ provides a mechanistic explanation for the later localization of failure potential and seismicity near the thermal front, rather than simply following the more widespread pressure perturbation.

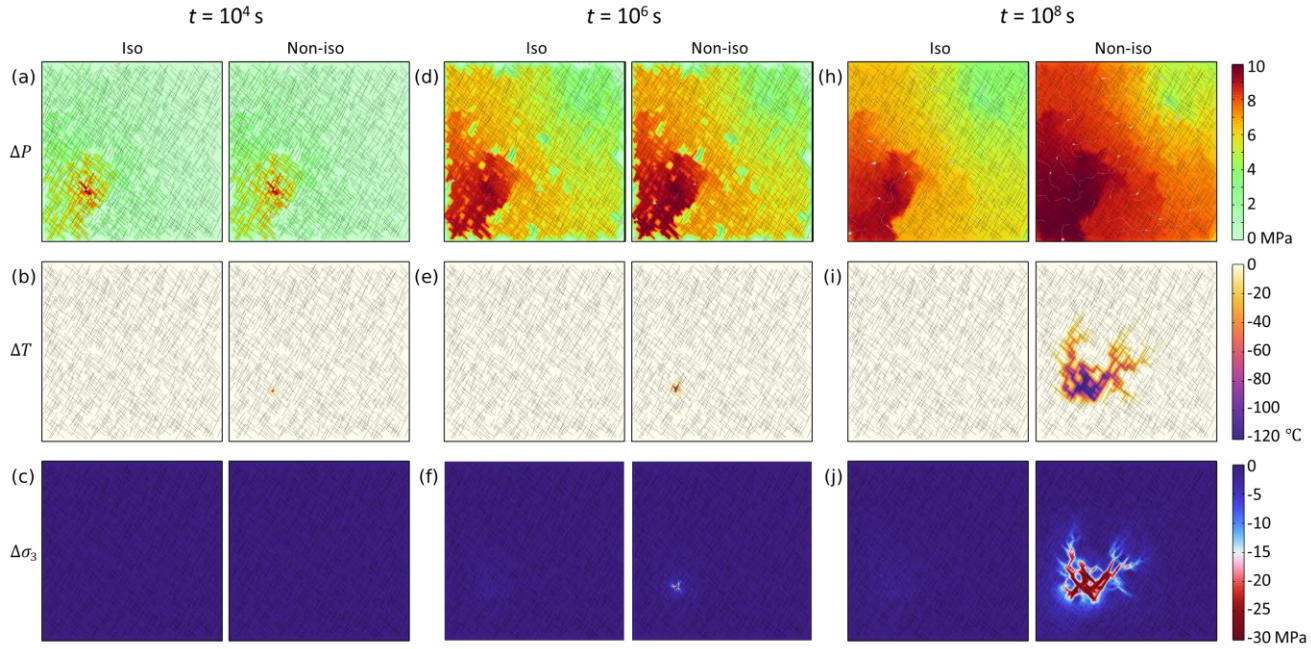

Figure 3: Spatiotemporal evolution of pressure, temperature, and stress fields in both scenarios.

3.3 Co-migration of Microseismicity with the Thermal Front

Figure 4 illustrates the spatial relationship among fracture ΔCFS, the evolving pressure and thermal fronts, and the distribution of dominant seismicity at representative times. At early time ($t \approx 10^6$ s), pressure perturbations have already propagated widely through hydraulically connected pathways, yielding a broad and relatively diffuse pressure pattern. Consistent with this distributed hydraulic influence, the selected high-moment events are scattered across multiple fracture clusters and do not form a coherent band. By intermediate time ($t \approx 10^6$ s), a more organized pattern begins to emerge: events increasingly concentrate in regions where ΔCFS is elevated, and the overall distribution becomes less diffuse than at early time. At late time ($t \gtrsim 10^8$ s, continuing to 3.2×10^8 s), this organization becomes pronounced. Elevated ΔCFS develops into a distinct, connected band within the fracture network, and seismicity clusters tightly within or immediately adjacent to this band. The event cluster also aligns closely with the advancing cold front, with the highest event density occurring near the thermal-front contour.

These observations indicate a transition in the dominant mechanism controlling the spatial organization of induced fracture slip and seismicity. Early in the injection, rapid pressure communication through a heterogeneous fracture network promotes a distributed response and therefore a relatively scattered seismicity pattern. As cooling progresses, thermoelastic stress changes increasingly govern where failure tendency concentrates: cooling modifies tractions by reducing effective normal stress and altering shear traction, producing a narrow zone of increased ΔCFS that co-migrates with the thermal front. The tight correspondence between dominant seismicity, elevated ΔCFS, and the cold front at intermediate to late times supports the interpretation that microseismicity can serve as a physically grounded tracer of thermal-front migration, whereas pressure perturbations alone cannot explain the observed late-time localization.

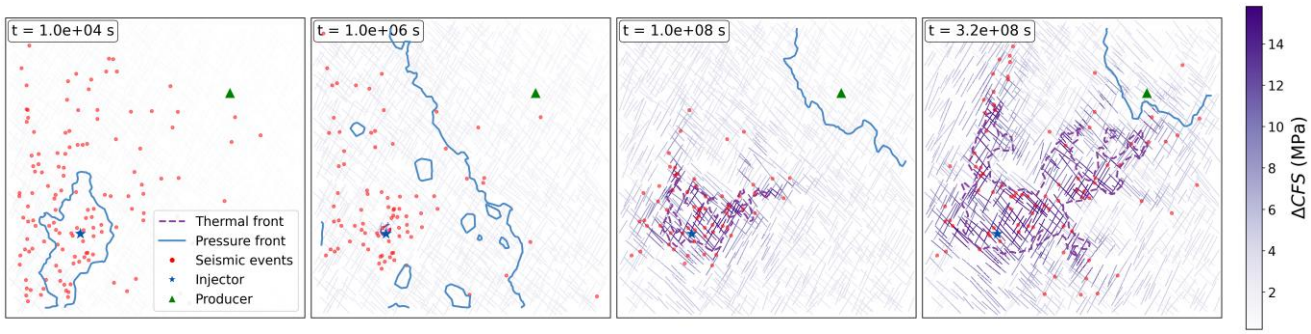

Figure 4: Spatial overlay of fracture ΔCFS, dominant seismicity, and propagating fronts.

Figure 5 compares the propagation distances of the pressure front, thermal front, and seismic front from the injector, with the injector–producer separation shown as a reference. The pressure front advances rapidly and monotonically, increasing from 140 m at 10^4 s to 670 m at 10^8 s, approaching the producer. In contrast, the thermal front migrates much more slowly, remaining within a few tens of meters of the injector at early times and reaching only 230 m by 10^8 s. The seismic-front distance evolves non-monotonically: it is comparatively large at early time but decreases markedly by $10^6 - 10^7$ s, and then increases again toward 10^8 s.

This non-monotonic behavior reflects the changing spatial organization of moment release over time. At early stages, pressure perturbations are widespread and the incremental moment release is distributed over many fractures, so that capturing the top 25% of total moment requires selecting a relatively large number of contributing fractures; the resulting event set therefore extends farther from the injector and yields a large seismic-front distance. As cooling develops, moment release becomes increasingly concentrated within the thermally stressed region near the migrating cold front, so the selected top-25% set becomes more spatially compact and the seismic-front distance shifts toward the thermal-front scale. At later times, continued advancement of the cold front and expansion of the cooling-influenced region drive renewed outward migration of the seismic front.

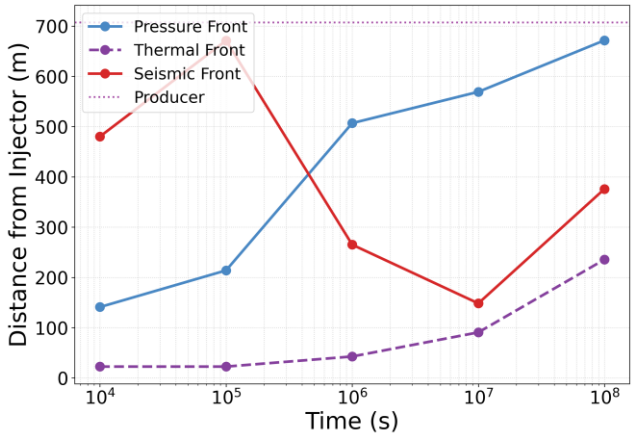

Figure 5: Temporal migration distances of pressure, thermal, and seismic fronts.

4. CONCLUSIONS

To conclude, induced seismicity progressively shifts from pressure-driven to cooling-dominated behavior, with seismic events tracking the migrating cold front.

1. The thermal contribution emerges at $\sim 10^4$ s, becomes comparable to the poroelastic contribution by $\sim 10^6$ s, and dominates at late time ($> 10^7$ s).

2. Pressure perturbations are broad and diffuse, whereas cooling is localized; the matrix minimum principal stress change closely overlaps the cooled domain, indicating thermoelastic control of stress evolution.

3. Fracture ΔCFS forms a narrow band that co-migrates with the thermal front. Consequently, dominant seismicity aligns more strongly with the cold front than the pressure front, supporting the hypothesis that microseismicity can serve as a proxy for tracking thermal migration.

Finally, in this study we considered a constant injection pattern. The system behavior could become more complicated if the extraction and injection control are varying, inducing pressure variations in time. Future work will need to address how these transient pressure signals interact with the thermal evolution.

ACKNOWLEDGMENTS

This work was supported by the Bilateral Cooperation Project between Flanders and China (grant number G0E5222N).

REFERENCES

Cao, W., Durucan, S., Shi, J.-Q., Cai, W., Korre, A., & Ratouis, T. (2022). Induced seismicity associated with geothermal fluids re-injection: Poroelastic stressing, thermoelastic stressing, or transient cooling-induced permeability enhancement? *Geothermics, 102*, 102404. https://doi.org/10.1016/j.geothermics.2022.102404

Cao, W., Durucan, S., Shi, J.-Q., Korre, A., Ratouis, T., & Hjörleifsdóttir, V. (2024). Geothermal fluid extraction and injection-related fracture slip susceptibility and seismicity in naturally fractured rocks. *International Journal of Rock Mechanics and Mining Sciences*, *183*, 105939. https://doi.org/10.1016/j.ijrmms.2024.105939

Chamarczuk, M., Ajo, J., Nayak, A., Norbeck, J., Latimer, T., Titov, A., & Dadi, S. (2025). Insights Into Seismicity Associated With Flexibly Operating Enhanced Geothermal System From Real-Time Distributed Acoustic Sensing. *Journal of Geophysical Research*.

Cuenot, N., Dorbath, C., & Dorbath, L. (2008). Analysis of the Microseismicity Induced by Fluid Injections at the EGS Site of Soultz-sous-Forêts (Alsace, France): Implications for the Characterization of the Geothermal Reservoir Properties. *Pure and Applied Geophysics*, *165*(5), 797–828. https://doi.org/10.1007/s00024-008-0335-7

Ganguly, S., & Mohan Kumar, M. S. (2014). Analytical solutions for movement of cold water thermal front in a heterogeneous geothermal reservoir. *Applied Mathematical Modelling*, *38*(2), 451–463. https://doi.org/10.1016/j.apm.2013.06.031

Gaucher, E., Schoenball, M., Heidbach, O., Zang, A., Fokker, P. A., Van Wees, J.-D., & Kohl, T. (2015). Induced seismicity in geothermal reservoirs: A review of forecasting approaches. *Renewable and Sustainable Energy Reviews*, *52*, 1473–1490. https://doi.org/10.1016/j.rser.2015.08.026

Jiang, C., Wang, X., Zhang, F., Deng, K., & Lei, Q. (2022). Fracture Activation and Induced Seismicity During Long-Term Heat Production in Fractured Geothermal Reservoirs. *Rock Mechanics and Rock Engineering*, *55*(8), 5235–5258. https://doi.org/10.1007/s00603-022-02882-z

Liu, L., Li, Y., Cao, W., Wang, T., Zhang, L., & Feng, X. (2025). Coupled thermo-hydro-mechanical-damage modeling of cold-water injection in deep geothermal reservoirs. *Journal of Rock Mechanics and Geotechnical Engineering*. https://doi.org/10.1016/j.jrmge.2025.03.005

Majer, E., Nelson, J., Robertson-Tait, A., Savy, J., & Wong, I. (2011). *Protocol for Addressing Induced Seismicity Associated with Enhanced Geothermal Systems (EGS)*.

Moein, M. J. A., Langenbruch, C., Schultz, R., Grigoli, F., Ellsworth, W. L., Wang, R., Rinaldi, A. P., & Shapiro, S. (2023). The physical mechanisms of induced earthquakes. *Nature Reviews Earth & Environment*, *4*(12), 847–863. https://doi.org/10.1038/s43017-023-00497-8

Rathnaweera, T. D., Wu, W., Ji, Y., & Gamage, R. P. (2020). Understanding injection-induced seismicity in enhanced geothermal systems: From the coupled thermo-hydro-mechanical-chemical process to anthropogenic earthquake prediction. *Earth-Science Reviews*, *205*, 103182. https://doi.org/10.1016/j.earscirev.2020.103182

Stopa, J., & Wojnarowski, P. (2006). Analytical model of cold water front movement in a geothermal reservoir. *Geothermics*, *35*(1), 59–69. https://doi.org/10.1016/j.geothermics.2005.11.002

Zhang, L., Dieudonné, A.-C., Daniilidis, A., Dong, L., Cao, W., Thibaut, R., Tas, L., & Hermans, T. (2025). Thermo-hydro-mechanical modeling of geothermal energy systems in deep mines: Uncertainty quantification and design optimization. *Applied Energy*, *377*, 124531. https://doi.org/10.1016/j.apenergy.2024.124531

Zhang, L., Mi, Z., Cao, W., Liu, L., Tas, L., & Hermans, T. (2025). Multi-objective optimization of energy efficiency and geomechanical safety in high-temperature aquifer thermal energy storage (HT-ATES) systems based on coupled thermo-hydro-mechanical (THM) analysis. *Energy*, 137096. https://doi.org/10.1016/j.energy.2025.137096